Appl. Magn. Reson. 14, 255–274 (1998)

Applied Magnetic Resonance

Influence of Hydrogen Bonds on the Electronic *g*-Tensor and ^{13}C-Hyperfine Tensors of ^{13}C-Labeled Ubiquinones – EPR and ENDOR Study

O. Nimz[1], F. Lendzian[1], C. Boullais[2], and W. Lubitz[1]

[1] Max-Volmer-Institut für Biophysikalische Chemie und Biochemie, Technische Universität Berlin, Berlin, Germany
[2] Département de Biologie Cellulaire et Moléculaire, SMM, CEA Saclay, Gif-sur-Yvette, France

Received August 15, 1997

Abstract. Selectively ^{13}C-labeled ubiquinone anion radicals in protic and aprotic solvents are investigated by EPR and ENDOR spectroscopy, yielding information about the effect of hydrogen bonds on the electronic *g*-tensor and the carbonyl carbon ^{13}C-hf tensors. Formation of the hydrogen bonds alter the *g*-tensor significantly to lower values and increases the A_{zz} component of the ^{13}C-hf tensor. Both effects can be explained by electrostatic interactions between the positively charged hydrogen and the electrons at the carbonyl oxygen leading to a redistribution of charge and π-spin density. Two different hydrogen bonds were obtained for $UQ_0^{-\bullet}$ which are in agreement with the results of DFT (density functional theory) calculations.

1. Introduction

Two quinone anion radicals, $Q_A^{-\bullet}$ and $Q_B^{-\bullet}$, play an important role in bacterial reaction centers (RC) as intermediates of the photosynthetic electron transfer chain in bacterial photosynthesis [1, 2]. The two quinones are identical in the RC of *Rhodobacter (Rb.) sphaeroides* (ubiquinone 10 [3]); however, they have different functional properties: Q_A functions as a one-electron gate, whereas Q_B accepts two electrons and two protons (like quinones under reductive conditions in protic solvent) and finally diffuses out of the RC. Crystallization of the RC from the species *Rhodopseudomonas (Rps.) viridis* and *Rb. sphaeroides* and subsequent X-ray crystallographic studies have determined the position and the surrounding amino acid residues of Q_A and Q_B [4]. These primary and secondary electron acceptors in RCs of *Rb. sphaeroides* have been trapped in their anion radical states in frozen RC solution, and their electronic structure has been investigated by EPR and ENDOR spectroscopy [1, 2]. The interaction with the protein surrounding, which regulates the quinone function as one- or two-elec-

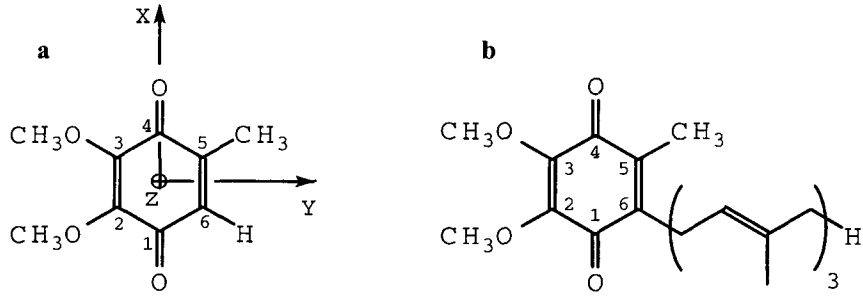

Fig. 1. Structure and numbering scheme of ubiquinones. **a** UQ_0, **b** UQ_3. Molecular axes, shown in **a** coincide with the *g*-tensor axes (see text) and ^{13}C-hf axes.

tron acceptors, is mainly caused by hydrogen bonds to the carbonyl groups. His(L190) and Ser(L233) were proposed from the X-ray structure [4] as likely H-bond donors for Q_B and His(M219) and the backbone NH of Ala(M260) for $Q_A^{-\bullet}$. π-interaction with the aromatic amino acid Trp(M252) has also been proposed for Q_A. FTIR measurements indicate strong H-bonds to the carbonyl oxygen at position 4 of Q_A [5, 6].

To investigate the influence of hydrogen bonding on the electronic structure of the primary and secondary electron acceptor, experiments with selectively ^{13}C-labeled ubiquinones reconstituted into the RC have been carried out [7, 8]. It has been found that values for the *g*- and ^{13}C-hyperfine (hf) tensors at positions 1 and 4 (see Fig. 1) are comparable to those found in isopropanol glass for $Q_B^{-\bullet}$; whereas, $Q_A^{-\bullet}$ shows a shift of the *g*-tensor principal component g_{xx}, and a large difference of the ^{13}C carbon spin densities at positions 1 and 4 [7, 8]. The asymmetric spin density distribution has been explained by an asymmetric binding pocket, namely by asymmetric H-bonding. To understand the influence of the H-bonds on the spin density distribution, experiments with continuous change in mole fraction of a mixed solvent in fluid solution were carried out [9, 10]. It has been shown that the isotropic ^{13}C-hfc constants (hfcs) at positions 1 and 4 (Fig. 1) of $UQ_0^{-\bullet}$ gradually shift from a small negative value in the aprotic medium to a small positive value in the protic medium. In this paper we will extend these studies to EPR and ENDOR experiments in frozen solution. The effects of hydrogen bond formation on the electronic *g*-tensor and on the carbonyl carbon ^{13}C-hyperfine tensors of $UQ_0^{-\bullet}$ and $UQ_3^{-\bullet}$ are investigated in detail by Q-band EPR. The hyperfine tensors of the hydrogen bond proton are determined by X-band cw ENDOR, which also allows the estimation of the respective bond lengths.

2. Experimental

UQ_0 and UQ_3, selectively ^{13}C-labeled at positions 1 and 4, were synthesized as described in [6]. The molecular structures of UQ_0 and UQ_3 are shown in Fig. 1.

2.1. Generation of the Anion Radicals $UQ_0^{-\bullet}$ and $UQ_3^{-\bullet}$

For samples in a protic medium the quinone anion radicals were generated by solving the quinone ($c \simeq 10^{-3}$ M) in anaerobic and slightly basic solutions of either protonated (IP-h_8) or fully deuterated (IP-d_8) isopropanol and adding a ten-fold excess of potassium *tert*-butylate. The samples were then shock-frozen in liquid nitrogen.

In aprotic solvent, the quinone anion radicals were generated by potentiostatically controlled electrolytic reduction, using tetra-n-butylammonium perchlorate ($\sim 10^{-2}$ M) as supporting electrolyte under high vacuum conditions in a self-built cell described elsewhere [11]. A mixture (2 : 1) of dimethoxyethane (DME) and methyltetrahydrofuran (MTHF) was used as solvent. Both solvents were purified, distilled and dried over liquid Na/K alloy on a high vacuum line. They were then distilled into the electrolysis cell from the high vacuum line. Electrochemical reduction was performed at room temperature under controlled potential using an Ag/AgCl reference electrode. The obtained semiquinone anion radical solution was transferred to the EPR capillary, which was finally sealed under high vacuum conditions.

2.2. Instrumentation

X-band EPR/ENDOR spectra were measured on a Bruker ESP-300E spectrometer using a laboratory-built ENDOR upgrade adapted to a nitrogen gas flow system for temperature control, described previously [12]. The extension for ENDOR consists of a Rhode and Schwarz radio frequency (rf) synthesizer (SMG) and an ENI solid state rf amplifier (A200L). The Q-band EPR spectra were measured on a Bruker ER200D EPR spectrometer equipped with a Bruker 051QR Q-band microwave bridge, a Bruker ER5103QTH resonator and an Oxford CF 935 cryostat.

2.3. EPR and ENDOR Data Analysis

In frozen solutions, anisotropic $\mathbf{g}$ and hyperfine interactions are, unlike in liquid solutions, not averaged out, and contributions of all molecular orientations relative to the magnetic field have to be considered. The spin Hamiltonian (in frequency units) including nuclei without quadrupolar interactions is then given by

$$\mathscr{H}_0 = \mu_B \mathbf{B}_0 \mathbf{g} \mathbf{S} - g_{ni} \mu_I \mathbf{B}_0 \mathbf{I}_i + h \mathbf{S} \mathbf{A}_i \mathbf{I}_i \,, \tag{1}$$

where $\mathbf{g}$ is the electronic g-tensor and $\mathbf{A}_i$ is the hf tensor of nucleus i consisting of the isotropic part $a_{iso} = 1/3\mathrm{Tr}\{\mathbf{A}_{ii}\}$ ($i = x, y, z$) and the traceless dipolar part $\mathbf{A}'$. $\mathbf{S}$, $\mathbf{I}_i$ and μ_B, μ_I are the electron and nuclear spin operators and magnetons, respectively, and $\mathbf{B}_0$ is the external field. The expressions for energy eigen values and EPR and NMR (ENDOR) transition energies are given in [13].

Signals from molecules with all possible orientations relative to $\mathbf{B}_0$ contribute to the EPR spectrum which is, therefore, significantly broadened due to the g- and hf tensor anisotropy. At Q-band (34 GHz) the g-tensor anisotropy of the quinone anion radicals is usually large compared to the proton hf tensor components, and the g-tensor principal values can be obtained from the turning points in the EPR powder type spectra. These EPR spectra have been analyzed on the basis of Eq. (1) by using a laboratory-written simulation and fit program based on the work of Rieger [14] using a modified Levenberg-Marquardt non-linear least-square model. This simulation routine includes second-order effects and can deal with an arbitrary number of nuclei with non-collinear g- and hf tensors [15, 16].

For the ENDOR transition frequencies in quinone anion radicals, the g-tensor anisotropy can be neglected in X-band. In this case the ENDOR resonance condition for nucleus i ($S = 1/2$, $I = 1/2$) is given by [13]

$$\nu_{\pm}^2 = \nu_n^2 + \frac{1}{4}(\mathbf{IAAI}) \mp \nu_n(\mathbf{IAI}) \quad , \tag{2}$$

where $\nu_{\pm}$ are the high and low frequency shifted ENDOR transitions, ν_n is the respective nuclear Zeeman frequency (14.4 MHz for a proton and 2.2 MHz for a deuteron at a magnetic field of 339 mT), $\mathbf{A}$ is the hf tensor, and $\mathbf{I}$ is the unit vector along the magnetic field with components $l_{x,y,z}$. For small hyperfine anisotropy of $\mathbf{A}$ ($|A_{ii} - A_{jj}|$, $|A_{ij}| \ll \nu_n$) Eq. (2) reduces to [17]

$$\nu_{\pm} = \nu_n \pm \frac{1}{2}(\mathbf{IAI}) \quad . \tag{3}$$

This equation is exact for orientations $\mathbf{B}_0$ parallel to either one of the principal axes (corresponding principal values A_{ii}, $i = x, y, z$) of $\mathbf{A}$. In frozen solution, peaks symmetrically displaced around ν_n are observed in the first derivative ENDOR spectra for each principal value A_{ii} ($i = 1, 2, 3$) of a hf tensor.

2.4. Hydrogen Bond Protons

In the case of a purely dipolar hf tensor, e.g., of a proton hydrogen bonded to an oxygen, the length of the respective hydrogen bond to the carbonyl oxygens can be estimated from the simple point-dipole approximation:

$$A'(\theta) = \frac{c}{r^3}\rho(3\cos^2\theta - 1) \quad , \tag{4}$$

where $A(\theta)$ is the hyperfine coupling expressed in MHz, $c = g\mu_B g_H \mu_H$ with g and g_H the electron and proton g-values and μ_B and μ_H the respective magnetons. ρ is the unpaired electron spin density at the oxygen, θ is the angle between the applied magnetic field $\mathbf{B}_0$ and the direction of the O-H bond and r is

the magnitude of the O-H distance vector in Å. For randomly oriented molecules one obtains pronounced features in the ENDOR spectrum corresponding to the inflection points of the absorption spectrum, which belong to orientations with $\theta = 0°$ and $\theta = 90°$. The signals have characteristic line shapes and the hf tensor principal values are related to each other by $A_{\parallel} = -2A_{\perp}$, $a_{iso} = 0$.

2.5. g-Tensor

According to the *g*-factor theory of Stone [18], the out-of-plane component of the *g*-tensor of planar semiquinone π radicals is equal to the free electron *g*-value, g_e, whereas the in-plane components are generally shifted by amounts Δg_{ii} towards higher values. This shift is determined by the spin-orbit induced mixing of the doublet ground state with excited doublet states. The high-field principal *g*-tensor value near 2.0023 is therefore assigned to the molecular *z*-axis (Fig. 1). For the assignment of the in-planes axes *x* and *y* an estimation of the dominant contribution is necessary. Δg_{xx} and Δg_{yy} in the quinones originates mainly from the excitation of an electron in a non-bonding lone-pair orbital on the carbonyl oxygen atoms into the half-occupied π^* orbital [18]. The wave function of a lone-pair orbital is described by superposition of s and p orbitals

$$\Psi_n^0 = c_s s + c_x p_x + c_y p_y \ , \tag{5}$$

where c_s and c_x, c_y measure the admixtures of the orbitals along the respective axes. The contributions to Δg are

$$\begin{aligned} \Delta g_{xx} &= 2\xi \rho_0^{\pi} c_y^2 / \Delta E_{n\pi^*} \ , \\ \Delta g_{yy} &= 2\xi \rho_0^{\pi} c_x^2 / \Delta E_{n\pi^*} \ , \end{aligned} \tag{6}$$

where is the ρ_0^{π} spin density on the carbonyl oxygen atom and $\Delta E_{n\pi^*}$ is the excitation energy from the non-bonding orbital n to the half-filled π orbital. ξ is the respective atomic spin orbit coupling constant, here for oxygen. The ratio $\Delta g_{yy}/\Delta g_{xx}$ equals c_x^2/c_y^2 and can be interpreted geometrically, assuming a trigonal arrangement of the three in-plane sp^2 oxygen orbitals. Since the symmetry axis of the oxygen lone pair n-orbitals forms angles of 60 and 30 degrees with the molecular *x*- and *y*-axes, respectively, Δg_{xx} is larger than Δg_{yy} [19].

2.6. Calculation of Spin Densities

In recent years *ab initio* methods for calculation of spin densities have become available using Density Functional Theory (DFT). For DFT calculations of spin densities we used the DMOL program [20] with the nonlocal spin density approximation BPW functional; i.e., the Perdrew and Wang generalized gradient approximation for the correlation functional [21] and the Becke gradient corrected

exchange functional [22] implemented by the DMOL program. After geometry optimization performed with a double-numerical basis set including polarization functions (DNP), with all electrons included in the self-consistent field (SCF) cycles, Mulliken spin densities were calculated. For modeling the influence of the protic environment, external water molecules were arranged close to the carbonyl groups of the energy minimized quinone structure.

Based on the obtained π-spin density distribution, calculations of purely dipolar hf tensors were carried out with a program that uses the method of McConnell-Strathdee [23].

3. Results and Discussion

3.1. Isotropic Liquid Solutions

The EPR spectra of non-labeled $UQ_0^{-\cdot}$ and $UQ_3^{-\cdot}$ in isotropic solution are presented in Fig. 2 in isopropanol (IP) and DME/MTHF, respectively. The spectra were analyzed by fitting using the program described above. The hfc values were

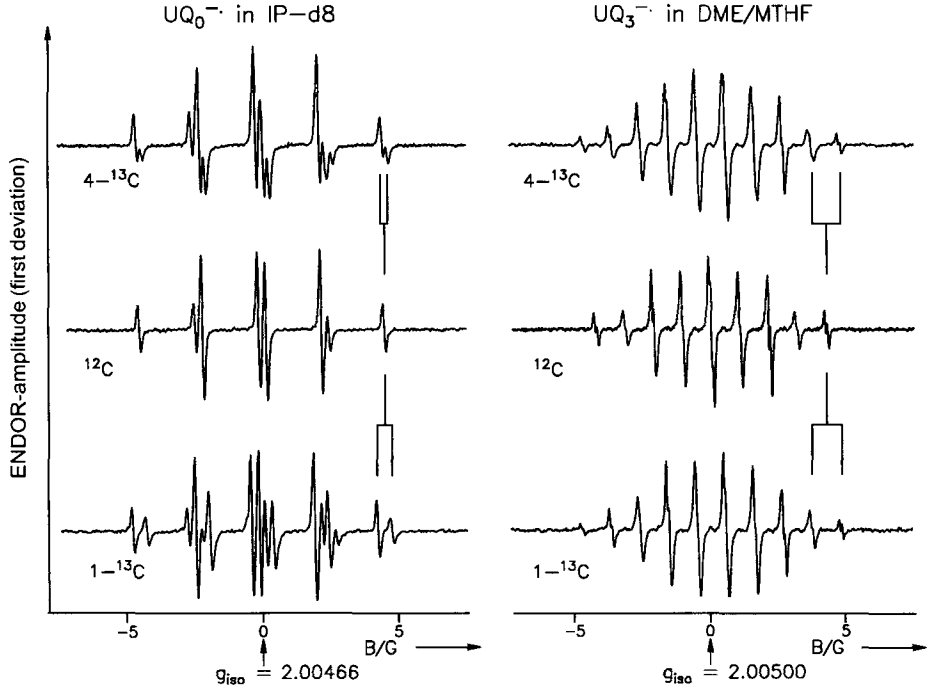

Fig. 2. EPR spectra of $UQ_0^{-\cdot}$ in fluid IP-d8 and $UQ_3^{-\cdot}$ in fluid DME/MTHF solution at 273 K. Experimental conditions: 0.2 mW microwave power (P_{MW}), 12.5 kHz field modulation, 0.05 G depth, accumulation time 1–10 min. The ^{13}C splittings are indicated for the high-field region of the spectra.

confirmed by ENDOR measurements in solution (spectra not shown). The spectral resolution of ENDOR is higher than that of EPR so that one additional small coupling due to the protons of the methoxy group could be resolved. The methyl proton hfc of $UQ_0^{-\bullet}$ increases and the α-proton hfc decreases in the protic solvent as compared with the aprotic solvent. In $UQ_3^{-\bullet}$ the hfcs of the methyl and β-protons are comparable to values measured for $UQ_{10}^{-\bullet}$ in IP [2, 24]. The hfc values of are nearly the same in IP and DME/MTHF. This indicates that formation of hydrogen bonds in $UQ_3^{-\bullet}$ is symmetric, while in $UQ_0^{-\bullet}$ asymmetric hydrogen bonds may induce an asymmetric spin density distribution. The g-factors of both molecules are decreased in protic compared to aprotic solution. The g-factors and hfc data are collected in Tables 1 and 2.

The π-spin density of carbons adjacent to α-protons are calculated from isotropic hfc values by using the McConnell equation [25]:

$$a_H = Q_{CH}\rho_C^{\pi} \ . \tag{7}$$

For β-protons the Heller-McConnell equation [26] is used:

$$a_{CH_3} = (B_1 + B_2\cos^2\theta)\rho_C^{\pi} \ , \tag{8}$$

where B_1 is usually assumed to be zero and $B_2 = 50$ G [13, 26, 31], and for free rotating methyl groups, $\cos^2\theta = 1/2$. The obtained spin densities are given in Section 3.2.6 (see Table 4).

In liquid solution the ^{13}C-hf coupling of the ^{13}C-labeled $UQ^{-\bullet}$ are obtained from cw EPR (Fig. 2). The spectra are analyzed by comparison with the spectra of non-labeled ubiquinone. The spectra of the ^{13}C-labeled UQ anion radicals show an interesting asymmetric linewidth effect. In protic solvent the low-field ^{13}C lines

Table 1. g-Tensor principal components for $UQ_0^{-\bullet}$ and $UQ_3^{-\bullet}$.

	g_{xx}	g_{yy}	g_{zz}	1/3Tr(**g**)	g_{iso}
$UQ_0^{-\bullet}$ IP-d8[a]	2.00613(5)	2.00526(5)	2.00210(5)	2.00450(5)	2.00466(1)
$UQ_3^{-\bullet}$ IP-d8[a]	2.00622(5)	2.00526(5)	2.00210(5)	2.00453(5)	2.00466(1)
$UQ_0^{-\bullet}$ IP-d8[b]	2.00622(5)	2.00532(5)	2.00219(5)	2.00458(5)	2.00469(1)
$UQ_3^{-\bullet}$ IP-d8[c]	2.00627(5)	2.00531(5)	2.00213(5)	2.00457(5)	—
$UQ_{10}^{-\bullet}$ IP-d8[d]	2.00646(5)	2.00542(5)	2.00222(5)	2.00470(5)	2.00469(1)
$UQ_0^{-\bullet}$ DME/MTHF[a]	2.00720(5)	2.00545(5)	2.00205(5)	2.00490(5)	2.00502(1)
$UQ_3^{-\bullet}$ DME/MTHF[a]	2.00700(5)	2.00537(5)	2.00202(5)	2.00480(5)	2.00500(1)

[a] This work, g-values from fits of the respective Q-band EPR spectra. Numbers in brackets are the errors in the last digit.
[b] W-band EPR g-values from [32] and isotropic X-band EPR g-value from [33].
[c] Q-band EPR g-values from [8].
[d] W-band EPR g-values from [19] and isotropic X-band EPR g-value from [33].

Table 2. ^{1}H-hf-tensor principal values (Gauss) of $UQ_0^{-\bullet}$ and $UQ_3^{-\bullet}$.

		A_{11}	A_{22}	A_{33}	1/3Tr(**A**)	a_{iso}[a]
$UQ_0^{-\bullet}$ IP-d8[b]	CH_3	1.7(1)	3.2(1)	1.7(1)	2.2	2.32(2)
	α-H	2.8(1)	0.1(1)	2.9(1)	1.9	2.05(2)
	1.HB[c]	−0.9(1)	2.0(1)	−0.9(1)	0.1	
	2.HB	−0.5(1)	2.0(1)	−0.5(1)	0.3	
$UQ_3^{-\bullet}$ IP-d8[b]	CH_3	1.9(1)	3.0(1)	1.8(1)	2.2	2.07(2)
	β-CH_2	≤0.7[d]	1.8(2)	≤0.7[d]		1.10(2)
	HB	−0.5(1)	2.0(1)	−0.5(1)	0.3	
$UQ_0^{-\bullet}$ DME/MTHF[b]	CH_3	1.8(1)	3.0(1)	1.8(1)	2.2	2.20(2)
	α-H	3.5(1)	0.1(1)	3.0(1)	2.2	2.19(2)
$UQ_3^{-\bullet}$ DME/MTHF[b]	CH_3	1.8(1)	2.9(1)	1.8(1)	2.2	2.09(2)
	β-CH_2[d]	≤0.7[d]	2.3(2)	1.5(2)		1.11(2)

[a] Isotropic hfcs from ENDOR at 273 K.

[b] Hf-tensor principal values obtained for the ^{12}C-compounds from X-band ENDOR and X- and Q-band EPR simulations (see text). Numbers in brackets are errors in the last digit. The CH_3-values for $UQ_3^{-\bullet}$ in IP compare well with those given for $UQ_{10}^{-\bullet}$ in IP in [24] (A_{11}: 1.7, A_{22}: 3.0, A_{33}: 1.7), and in [29] (a_{iso} = 2.08). Values for $UQ_3^{-\bullet}$ in DME compare well with those given for $UQ_{10}^{-\bullet}$ in DME [2, 29] ($a_{iso}(CH_3)$ = 2.10 and 2.11, and a_{iso}(β-CH_2) = 1.04 and 1.06). The EPR simulations indicate that the A_{33}-axis is close to the molecular z-axis; the A_{22}-axis of CH_3 is approximately 30° from the y-axis in $UQ_0^{-\bullet}$ and $UQ_3^{-\bullet}$ in and the A_{22}-axis of the α-H in $UQ_0^{-\bullet}$ is 10° from the y-axis.

[c] Hf-tensor values from hydrogen bonded protons (HB) from ENDOR. The two smaller components (A_{11} and A_{33}) are assumed to be negative. Two symmetrical bonds are assumed for $UQ_3^{-\bullet}$. Oxygen-hydrogen distances according to Eq. (4) with ρ_0^π = 0.22 are: 1.86 and 1.90 Å for CO_1 and CO_4 of $UQ_0^{-\bullet}$, respectively and 1.96 Å for $UQ_3^{-\bullet}$ (see text).

[d] Estimated upper limits for A_{11} and A_{33} from the EPR simulations.

are narrower than the corresponding high-field ^{13}C lines. In aprotic solvent the opposite linewidth variation is obtained (see Fig. 2). This effect may be used to determine the sign of the isotropic ^{13}C-hfc. According to [13, 27, 28] the width of a single EPR line in liquid solution has contributions:

$$\frac{1}{T_2} = A + Bm_I + Cm_I^2 \quad . \tag{9}$$

Here, T_2 is the transverse electron spin relaxation time and m_I is the nuclear magnetic quantum number. The coefficients A ... C are related to tensor products of the anisotropic interactions [13, 27, 28]:

$$A = \frac{2}{15}\left(\frac{\mu_B B_0}{\hbar}\right)^2 (\mathbf{g}':\mathbf{g}')\,\tau_c \quad , \tag{10a}$$

$$B = \frac{4}{15}\left(\frac{\mu_B B_0}{\hbar}\right)(\mathbf{g}':\mathbf{A}')\,\tau_c \quad , \tag{10b}$$

$$C = \frac{2}{15}(\mathbf{A}':\mathbf{A}')\,\tau_c \quad , \tag{10c}$$

where μ_B and B_0 are Bohr's magneton and the applied static magnetic field; $\mathbf{g}'$ and $\mathbf{A}'$ (in frequency units) are the purely anisotropic parts of the g- and hyperfine tensors, and τ_c is the rotational correlation time of the tumbling motion of the molecule in liquid solution.

The asymmetric linewidth effect is caused by the term linear in m_I in Eq. (9). Since we have determined the g- and ^{13}C-hf tensors (see below), we can determine the sign of the coefficient B (Eq. (10b)). From Tables 1 and 3 the components of the anisotropic tensors are obtained as g'_{xx}, $g'_{yy} > 0$, $g'_{zz} < 0$ and A'_{xx}, $A'_{yy} < 0$, $A'_{zz} > 0$. Therefore $(\mathbf{g}':\mathbf{A}')$ and hence B are <0. According to Eq. (9), the narrower EPR line is then observed for transitions connecting $m_I = +1/2$ spin levels, whereas transitions connecting $m_I = -1/2$ levels should be broadened. For positive isotropic ^{13}C-hfc the $m_I = +1/2$ transition is shifted to low field. Since in protic solvent the low-field ^{13}C EPR line is narrower compared with the high-field component (see Fig. 2), the sign of the corresponding isotropic ^{13}C-hfc must be positive. A negative ^{13}C-hfc is obtained for aprotic solvent. The isotropic ^{13}C-hfcs, including signs obtained from the EPR spectra, are shown in Table 2. They agree well with the values published for (4-^{13}C) ubisemiquinone-10 [29]. ENDOR experiments were performed in liquid solutions yielding accurate values for the proton hfcs given in Table 2. ^{13}C-ENDOR resonances for ^{13}C positions 1 and 4

Table 3. 1- and 4-^{13}C-hf-tensor principal values (Gauss).[a]

	A_{xx}	A_{yy}	A_{zz}	1/3Tr(**A**)[b]	a_{iso}[c]
1-^{13}C $UQ_0^{-\cdot}$ IP-d8	−4.9(8)	−4.1(8)	+9.7(2)	+0.2	+0.50(2)
4-^{13}C $UQ_0^{-\cdot}$ IP-d8	−5.1(8)	−4.5(8)	+10.5(2)	+0.3	+0.20(2)
1-^{13}C $UQ_0^{-\cdot}$ DME/MTHF	−3.3(8)	−4.5(8)	+8.5(2)	+0.2	−1.40(2)
4-^{13}C $UQ_0^{-\cdot}$ DME/MTHF	−4.0(8)	−5.7(8)	+7.5(2)	−0.7	−1.30(2)
1-^{13}C $UQ_3^{-\cdot}$ IP-d8[d]	−4.0(8)	−4.9(8)	+10.0(2)	+0.0	+0.40(2)
4-^{13}C $UQ_3^{-\cdot}$ IP-d8[d]	−4.5(8)	−5.0(8)	+11.0(2)	+0.5	+0.70(2)
1-^{13}C $UQ_3^{-\cdot}$ DME/MTHF	−4.3(8)	−5.4(8)	+7.3(2)	−0.8	−1.15(2)
4-^{13}C $UQ_3^{-\cdot}$ DME/MTHF	−4.7(8)	−5.5(8)	+7.3(2)	−1.0	−1.15(2)

[a] Values from fits of the X- and Q-band EPR spectra of ^{13}C-labeled $UQ_0^{-\cdot}$ and $UQ_3^{-\cdot}$ (compare Fig. 5). Numbers in brackets are estimated errors in the last digit. Values for A_{zz} are fairly accurate due to the resolved ^{13}C splitting of the g_{zz} component. For A_{xx} and A_{yy} the errors are larger. ^{13}C-hf tensor axes coincide with g-tensor axes.

[b] 1/3Tr(**A**) is the isotropic part obtained from the full tensor.

[c] a_{iso} is the isotropic hfc measured in liquid solution with generally good agreement concerning magnitudes and signs of a_{iso} measured independently in [9, 10, 29] for $UQ_0^{-\cdot}$ and $UQ_{10}^{-\cdot}$ in alcohols and DME.

[d] Values from [8]: −4.3, −3.7, +10.9 and −4.0, −3.5, +11.5 for A_{xx}, A_{yy}, A_{zz} of 1-^{13}C and 4-^{13}C $UQ_3^{-\cdot}$, respectively. Similar values were reported for A_{zz} of $UQ_{10}^{-\cdot}$ in [7]: 11.3 and 11.0 for 1-^{13}C and 4-^{13}C, respectively.

of the molecules could not be detected in the accessible temperature range (150–330 K) limited by solvent properties.

3.2. Anisotropic Interactions in Frozen Solution

3.2.1. *g*-Tensor

g-Tensors of different substituted quinone anion radicals in protic solvents have been measured with high accuracy using high-field EPR [19]. Interestingly, the authors observed a *g*-tensor shift for the duroquinone anion radical in aprotic and protic solvents. Here, we investigate this effect in more detail for two ubiquinone anion radicals.

Figure 3 shows the Q-band EPR spectra of ubiquinone anion radicals ($UQ_0^{-\cdot}$ and $UQ_3^{-\cdot}$) in the protic (IP) and the aprotic solvent (DME/MTHF). The spectra were

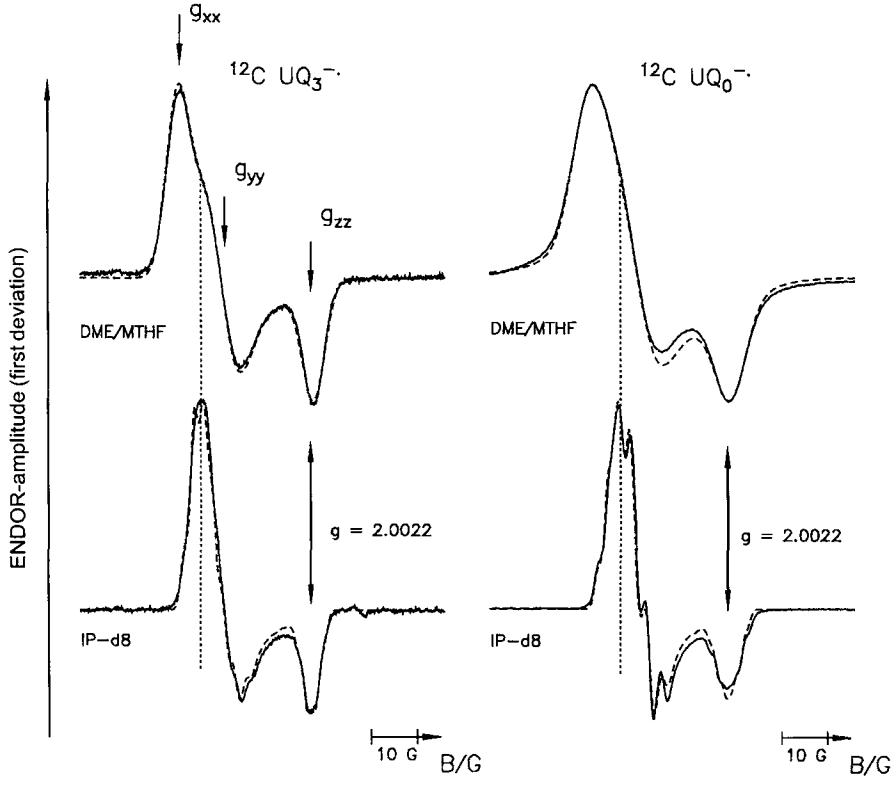

Fig. 3. Q-band (34 GHz) spectra of non-labeled $UQ_3^{-\cdot}$ and $UQ_0^{-\cdot}$ (ca. 10^{-3} M) in frozen deuterated IP-d8 and DME/MTHF solution. Experimental conditions: P_{MW} = 2.5 μW, 12.5 kHz field modulation, 0.25 G depth, accumulation time 13 min, T = 70 K. Dashed traces are best simulations (see text).

analyzed by simulation and fitting of the Q-band EPR powder spectra using the ^1H-hf tensors from ENDOR (see below) and a basic Gaussian linewidth of 0.7 Gauss due to additional weak unresolved ^1H interactions. The best simulations are shown as dashed traces in Fig. 3. The resulting g-tensors are given in Table 1.

In both radicals the g_{xx} component is significantly shifted towards larger values in the aprotic environment. The observed g_{xx} shift is attributed to formation of hydrogen bonds to the carbonyl oxygens in the protic solvent, which causes two effects. (i) The positive charge of the bridging hydrogen is compensated by an increased negative partial charge at the oxygen which decreases the spin density ρ_0^π and increases the spin density at ρ_C^π of the carbonyl carbon [8, 24]. (ii) The formation of a hydrogen bond to an oxygen lone-pair n orbital increases $\Delta E_{n\pi^*}$ in Eq. (6) by lowering the energy of the lone-pair orbital. Thereby spin orbit induced admixture of the n orbital to the half-filled π^* orbital is reduced.

Both effects are expected to lower the values of g_{xx} and g_{yy} (more precisely, $\Delta g_{xx} = g_{xx} - g_e$ and $\Delta g_{yy} = g_{yy} - g_e$). g_{xx} is more strongly affected since the lone-pair orbital is closer to the y-axis (see above and [19]). The decrease of the g_{xx} component due to hydrogen bonding in the protic solvent is more pronounced in $UQ_0^{-\bullet}$ than in the anion radicals with an isoprenoid chain, $UQ_3^{-\bullet}$. This indicates stronger hydrogen bonding for $UQ_0^{-\bullet}$.

The decrease of Δg_{xx} in the protic solvent, resulting from the reduction of spin density of the carbonyl oxygen, $\Delta\rho_0^\pi$, can be estimated from the ^{13}C-hf tensors in IP and DME/MTHF (see below). It is about one half of the observed shift Δg_{xx}. The second contributing effect, increase of $\Delta E_{n\pi^*}$, is therefore of comparable magnitude. The observed shift of the isotropic g-value in liquid solution (see above) is in agreement with the shifts of the g-tensor principal values observed in frozen solutions.

3.2.2. Hf Tensors from Protons Directly Attached to the Ubiquinones

In frozen solutions and using a non-selective field setting in the EPR, the ENDOR spectrum shows proton resonances covering the entire range of the anisotropic hf-tensor principal values. In quinones the coupling to the large spin density on the carbonyl oxygen leads to an unusually large anisotropy of the methyl proton coupling, which differs from the generally small anisotropy of methyl protons [24]. The hf-tensor principal values can be obtained from the turning points in the frozen solution powder-type ENDOR spectrum. In the asymmetrically substituted ubiquinones the spectral features of different overlapping protons were obtained by simulation of the ENDOR spectra and by comparison with monosubstituted quinones. In addition, the g-tensor anisotropy was used for an orientation selection via the magnetic field setting.

Unlike in liquid solution, purely dipolar resonances of surrounding solvent protons are not averaged out but contribute to the spectra. These resonances can be discerned by using fully deuterated IP-d8. Thereby, ENDOR lines of solvent

deuterons are shifted towards lower frequencies due to the ~6.5 times smaller nuclear Zeeman frequency as compared with protons.

Figure 4 shows the frozen solution ENDOR spectra of $UQ_0^{-\bullet}$ in IP-h8 (A) and IP-d8 (C). Spectrum C is dominated by the methyl proton hyperfine tensor. Contributions of the α-proton (position 6, Fig. 1) were obtained by orienta-

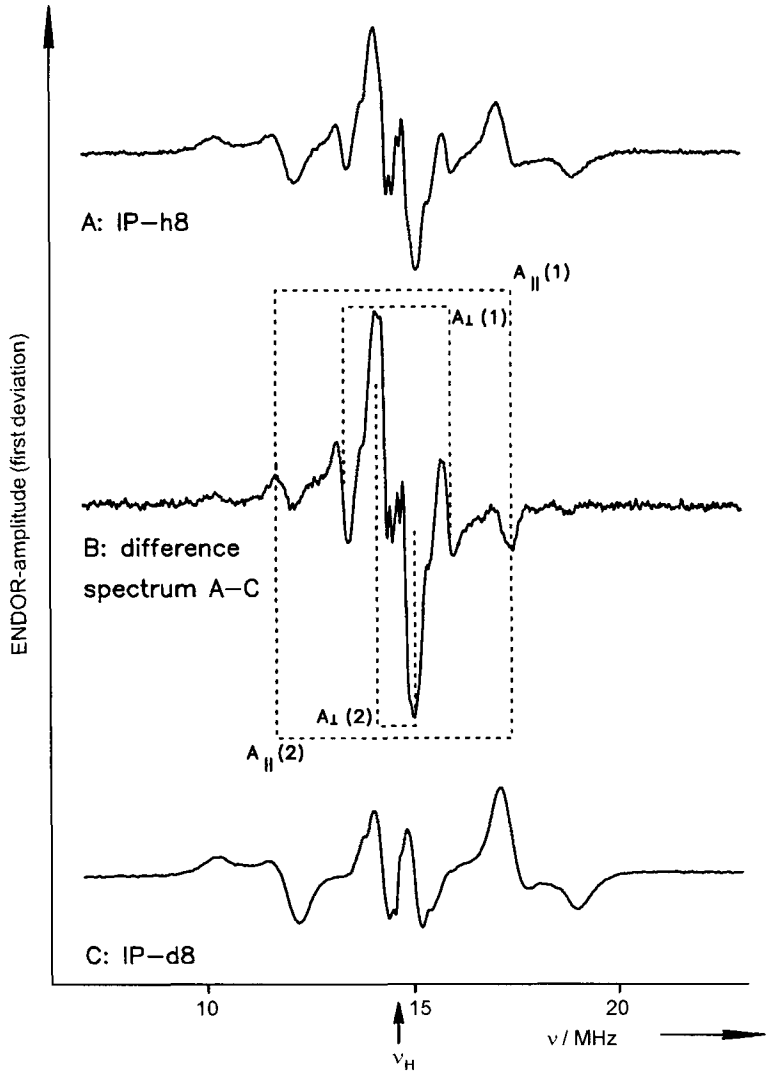

Fig. 4. ^{1}H-ENDOR spectra of ^{12}C-$UQ_0^{-\bullet}$ (ca. 10^{-3} M) in frozen protonated (A) and fully deuterated propan-2-ol solution (C), B – difference spectrum. Experimental conditions: 50 W radio frequency power (P_{RF}), P_{MW} = 4 mW, 12.5 kHz frequency modulation, deviation: ±70 kHz, T = 123 K, accumulation time 30 min. Spectral components in C assigned to two different couplings from hydrogen bond protons are indicated ($A_{\parallel}(1)$, $A_{\perp}(1)$, $A_{\perp}(2)$).

tion-selected ENDOR at the edges of the EPR spectrum (spectra not shown). The obtained values were corroborated by simulation of the EPR powder spectra in Q- and X-band (see below). The anisotropic hf tensor of the α-proton is in agreement with values calculated according to McConnell-Strathdee [23] and using the carbon and oxygen π-spin densities given below. The ENDOR spectra measured in aprotic solvent (DME/MTHF) exhibited similar shapes as in Fig. 4, spectrum C and are therefore not shown. Similar ENDOR spectra were also obtained for $UQ_3^{-\bullet}$ in IP. All ^1H-hf tensor data are given in Table 2. Only a very small change of A_{11} is observed for the α-proton of $UQ_0^{-\bullet}$ when comparing protic and aprotic solvents. For $UQ_3^{-\bullet}$ no change is observed for the CH_3^- and β-CH_2 protons. This shows that hydrogen bonding to both carbonyl groups does not change the spin densities at positions 2,3 and 5,6 within experimental error (see Fig. 1).

3.2.3. Hf Tensors from Hydrogen-Bonded Protons

The additional spectral features of solvent protons in protonated isopropanol are obtained by subtracting the spectra in protonated and in fully deuterated isopropanol. The difference spectrum (Fig. 4, spectrum B) shows only lines from solvent protons, the larger hfc's are assigned to hydrogen bonds. For $UQ_0^{-\bullet}$ there are two features that can be assigned to two $A_\perp$ components ($A_\perp(1)$ and $A_\perp(2)$) and only one feature with a shape expected for an $A_\parallel$ component of an axially symmetric tensor. Combination of $A_\parallel(1)$ and $A_\perp(1)$ results in one purely dipolar interaction with values similar to those found for the benzoquinone radical anion ($BQ^{-\bullet}$) [24]. The $A_\parallel(2)$ of the second hydrogen bond could be hidden under $A_\perp(2)$ or could have the same value as $A_\parallel(1)$. By comparison with the results for UQ_{10} and duroquinone anion radicals [24] we prefer the latter interpretation. In this case, combination of the $A_\parallel(2)$ and $A_\perp(2)$ components yields a hf tensor of the second H-bond which is very similar to those in $DQ^{-\bullet}$ and $UQ_{10}^{-\bullet}$. Its small isotropic contribution has been explained by a geometric distortion due to steric hindrance caused by the bulky CH_3 group. In Table 2 the hf-tensor data of the hydrogen bonds for $UQ_0^{-\bullet}$ as well as for $UQ_3^{-\bullet}$ are summarized.

3.2.4. Hydrogen Bond Distances

The hydrogen bond distances may be estimated according to Eq. (4) assuming ρ_0^π to be 0.22, which was obtained from the hf couplings in ^{17}O-labeled $BQ^{-\bullet}$ and $DQ^{-\bullet}$ [24]. The distances in Å obtained from this point-dipole model analysis are included in Table 2. In principle, a McConnel-Strathdee calculation of the H-bond proton hf tensor should yield more accurate distances provided the H-bond geometry is known. Since this is not known – and even a distribution of different geometries could be present – the simple point-dipole model was used for our estimates.

3.2.5. ^{13}C-hf Tensors

The ^{13}C-hf tensors in frozen solution were measured by cw EPR in Q- and X-band. The *g*-tensor of ubiquinone anion radicals is sufficiently anisotropic to allow sepa-

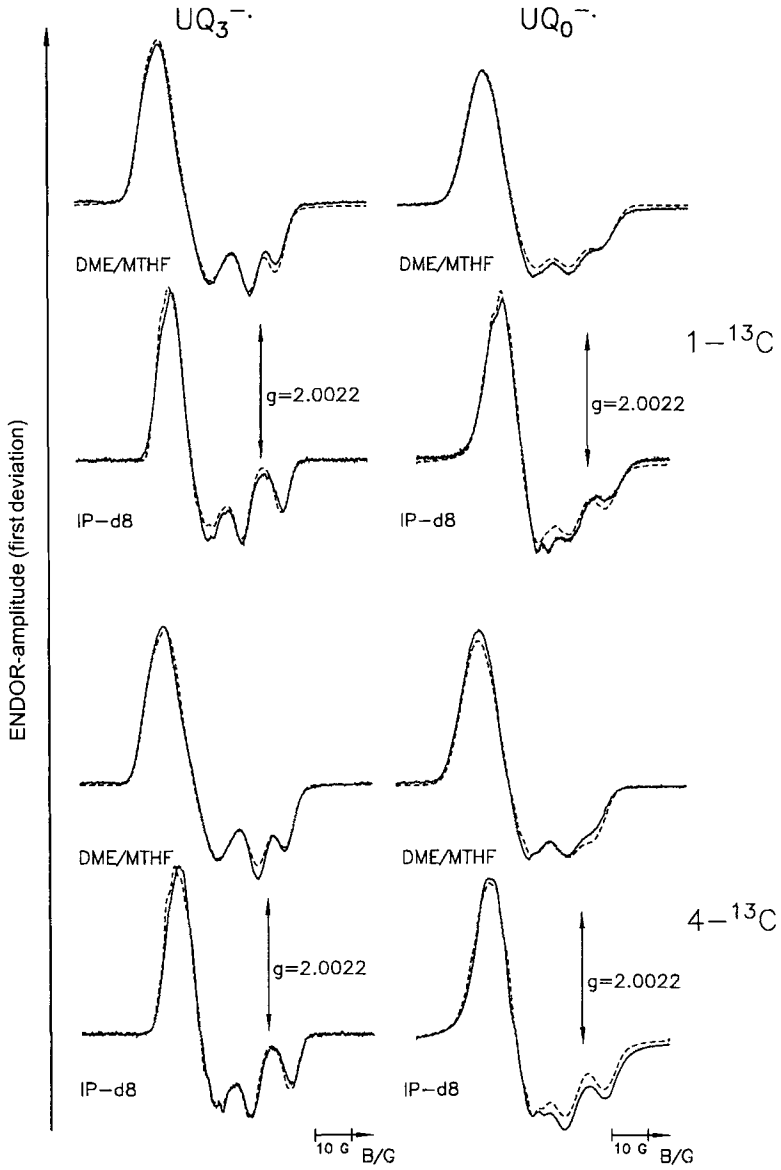

Fig. 5. Q-band (34 GHz) EPR spectra of 1- and 4-^{13}C-labeled $UQ_3^{-\cdot}$ and $UQ_0^{-\cdot}$ (ca. 10^{-3} M) in frozen DME/MTHF and deuterated propan-2-ol solution. Experimental conditions: P_{MW} = 2.5 μW, 12.5 kHz field modulation, 0.25 G depth, accumulation time 30 min, T = 70 K. Dashed traces show best fits.

ration of the principal values assigned to the molecular axes (x, y, z) in Q-band, see Fig. 3. The ^{13}C hyperfine splitting along the molecular z-axes is clearly resolved in the Q-band spectra. The spectral regions of g_{xx} and g_{yy} are broadened in comparison with the unlabeled $UQ^{-\bullet}$. For determination of the full ^{13}C tensor, the Q-band EPR powder spectra were fitted. Thereby the coupling-tensors of all protons, including hydrogen bonds to the deuterated solvent as obtained from X-band EPR and ENDOR measurements with non-labeled $UQ^{-\bullet}$, were kept constant. The experimental and fitted Q-band EPR powder spectra are shown in Fig. 5 for $UQ_3^{-\bullet}$ and $UQ_0^{-\bullet}$. The obtained ^{13}C-hf tensor principal values are collected in Table 3. The A_{zz} hf-tensor components of the ^{13}C tensor are significantly smaller for all $UQ^{-\bullet}$ in the aprotic as compared with the protic solvent. This demonstrates that formation of H-bonds increases the spin density on the carbonyl carbons. The A_{xx} and A_{yy} components are quite similar in both solvents. However, these values are less accurate (see Table 3). The A_{zz} hf-tensor component in the aprotic solvent in $UQ_3^{-\bullet}$ is identical for positions 1 and 4, while in $UQ_0^{-\bullet}$ the A_{zz} component in position 1 is larger than in position 4. This indicates an asymmetry of the spin density distribution in case of $UQ_0^{-\bullet}$ based on the different geometry and substituents. In protic solvent (IP) the A_{zz} hf tensor component at position 4 (Fig. 1) is in both radicals, $UQ_0^{-\bullet}$ and $UQ_3^{-\bullet}$, larger than in position 1. Also, a larger difference between the A_{zz} hf tensor components in aprotic and protic solvent is found for position 4. Thus, the influence of H-bond formation on the spin density redistribution is stronger in the neighborhood of the methyl group. This is somewhat surprising for $UQ_0^{-\bullet}$, because this position is sterically hindered compared with position 1, and one might expect a larger effect for the shorter H-bond.

3.2.6. Determination of ^{13}C π-Spin Densities. p_z-Spin Densities from the Experiments

In a previous EPR study of $UQ_{10}^{-\bullet}$ in liquid solution ^{13}C π-spin densities were estimated from the isotropic hfcs [29] using the procedure of Fraenkel and Karplus [30]. However, since the isotropic ^{13}C-hfc is determined by π-σ spin polarization from neighboring carbon and oxygen atoms, and different contributions with opposite signs cancel each other, the ^{13}C π-spin densities obtained in this way depend strongly on the spin densities of the neighboring atoms (ring carbons and oxygens), which are not exactly known. Therefore we prefer to estimate the carbonyl ^{13}C π-spin densities from the purely dipolar part of the hf tensor, $\mathbf{A}'$, with the theoretical calculated principal values ($-a_0$, $-a_0$, $2a_0$) for a carbon ($|a_0| = 38.32$ G [31] which carries a p_z-spin density of $\rho_C^\pi = 1$. The observed hf coupling consists of isotropic and additional anisotropic contributions,

$$A_{ii} = A'_{ii} + a_{\text{iso}} \qquad (i = x, y, z) \; . \tag{11}$$

The purely dipolar parts, A'_{ii}, were obtained from the principal values, A_{ii}, measured by Q-band EPR by subtracting the isotropic part (1/3Tr$\mathbf{A}$), including signs.

The influence of oxygen and ring carbon π-spin densities on the spectroscopically best characterized A_{zz} component was estimated by a McConnel-Strathdee calculation [26]. For this purpose we calculated the hf tensors of carbonyl carbon positions 1 and 4 with a model containing only the π-spin densities of the ring carbons determined independently by ENDOR which results in a contribution along the z-axis of −0.2 G. Additionally, the neighboring carbonyl oxygens with $\rho_0^\pi = 0.22$ contribute to A_{zz} by approximately −0.4 G. The A'_{zz} component was corrected by these contributions from neighboring atoms and from this value ρ_C^π was obtained for C1 and C4 using $|A'_{zz}| = 2|a_0|\rho_C^\pi$. The carbon π-spin densities are given in Table 4.

We found that the carbonyl carbon spin densities in protic solvent (IP) are all larger than in the aprotic environment (DME/MTHF). Thus, the formation of hydrogen bonds leads to a significant increase of carbonyl carbon spin density. In $UQ_3^{-\bullet}$ equal ^{13}C spin densities are found for C1 and C4 in aprotic solvent. They increase by 60–70% in protic solvent with a slightly higher value for C4.

In $UQ_0^{-\bullet}$ a larger ^{13}C spin density is found for C1 as compared with C4 in the aprotic solvent. This is more clearly seen from the respective A_{zz} components (Table 3). This asymmetry results from the asymmetric substituents, CH_3 and H at positions 5 and 6, respectively. Also, the spin densities at both carbonyl car-

Table 4. Comparison of calculated spin densities (DFT) and values estimated from the anisotropic ^{13}C-hf tensors.

		C1	C2	C3	C4	C5	C6	O1	O4
$UQ_0^{-\bullet}$[a]	ρ_{2p_z}	0.090	0.047	0.059	0.107	0.084	0.082	0.220	0.229
	ρ_{3p_z}	0.012	0.006	0.005	0.0012	0.005	0.006	0.000	0.000
$UQ_0^{-\bullet}$[b]	ρ_{2p_z}	0.110	0.046	0.063	0.129	0.069	0.077	0.207	0.211
	ρ_{3p_z}	0.012	0.006	0.005	0.012	0.006	0.006	0.000	0.000
$UQ_0^{-\bullet}$[c]	in DME/MTHF	0.099			0.098	0.088	0.081		
	in IP	0.115			0.124	0.093	0.076		
$UQ_3^{-\bullet}$[c]	in DME/MTHF	0.076			0.074	0.084			
	in IP	0.121			0.128	0.083			

[a] Calculated spin densities from DMOL using Mulliken analysis for the energy-optimized structure of $UQ_0^{-\bullet}$.

[b] Calculated spin densities from DMOL using Mulliken analysis (see [34]) for the optimized structure of $UQ_0^{-\bullet}$ with two water molecules attached in plane of the molecule with one H-bond along the symmetry axis of the non-bonding orbital of the oxygen directed towards the side of the methyl group. O..H distance: 1.8 Å. The s-spin density, ρ_s, of the α-proton is −0.006 and the H-bonding protons have ρ_s values of 0.000 in plane and up to 0.002 when the hydrogen bond is rotated 45° out of the UQ_0 plane (see text).

[c] Spin densities for C1 and C4 calculated from the experimental dipolar ^{13}C-hf tensor component A'_{zz} (Table 3) corrected by the contributions of neighboring carbons and oxygen. About 40% larger values are calculated in [29] from the isotropic hfc using the Karplus/Fraenkel approach (see text). C5 and C6 are calculated from the isotropic hfc of Table 2 using the McConnell and Heller-McConnell equation with $Q_H = -27$ G and $B_2 = 50$ G (Eqs. (7), (8)).

bons are larger than those in $UQ_3^{-\bullet}$. In the protic solvent the shifts of spin densities at C1 and C4 are not quite as large as for $UQ_3^{-\bullet}$. However, a stronger increase of spin density is observed for C4, which now has a larger value than that for C1. This indicates two different hydrogen bonds for $UQ_0^{-\bullet}$, which is supported by the ENDOR experiments which yield two different hydrogen bond lengths (see Table 2).

3.2.7. Density Functional Calculations

Geometry. The energy optimized structure of $UQ_0^{-\bullet}$ is characterized by a planar ring and bond distances of 1.29 Å for the carbonyl and 1.46 Å for the C1-C2 and 1.39 Å for C2-C3 bond length. The methoxy groups are arranged trans to the ring plane and exhibit an out-of-plane twist angle of 57°.

Spin Densities. We find an overall excellent agreement between calculated (DFT) and experimental π-spin densities. The DFT calculations for $UQ_0^{-\bullet}$ predict π-spin densities of carbons adjacent to the α-proton (C6) and to the methyl group (C5) which agree very well with those obtained from experiments in aprotic solution using Eqs. (7) and (8) with Q factors of $Q = -27$ G and $B_1 = 0$, $B_2 = 50$ G for α- and β-protons, respectively. Also, the isotropic hfc of the α-proton is in good agreement with the calculated value based on the hydrogen s-spin density and using the structure-independent Q factor of 1420 MHz.

Furthermore, the calculated p_z-spin densities for the oxygens agree well with the experimental value for $DQ^{-\bullet}$ [24].

The calculated π-spin densities for the carbonyl carbon position C4 is approximately 20% larger than the corresponding value for position C1. However, the experimental ^{13}C-hf-tensor component A_{zz} shows an opposite behavior (Tables 2 and 3).

To calculate the effects of H-bonds, two water molecules were attached to the $UQ_0^{-\bullet}$ structure (see Table 4, footnote). This results in decreased calculated π-spin densities of the oxygens and the calculated π-spin densities at the carbonyl carbons increased by an amount similar to that observed in the experiments.

Interestingly, the experimentally obtained shift of ^{13}C π-spin density at C4 (+27%) is larger than that found for C1 (+16%) as concluded from the experiments. The two different hf tensors found for the H-bond protons in $UQ_0^{-\bullet}$ (Table 2) further support this asymmetry with respect to the hydrogen bonding. The isotropic contribution to the hf tensor of the weaker bonded proton might result from direct orbital overlap with the oxygen p_z-orbital, if the H-bond is assumed to be bent out of the molecular plane of $UQ_0^{-\bullet}$. When the angle between the ring plane and the H-bond to the carbonyl next to the methyl group was increased successively from 0 to 90°, an increase of the calculated DFT π-spin density ρ_C^{π} at C4 of up to 10% was observed. For C1, with an unchanged H-bond geometry, a concomitant decrease of comparable magnitude is obtained.

The spin densities of the other carbon positions are not significantly influenced. The calculations also yield a small positive s-spin density for the H-bond proton up to 0.002, if the H-bond is bent 45 degrees out of the quinone plane, which is in qualitative agreement with the observed isotropic contribution of the respective hf tensor. These results lead to a consistent interpretation of the hf data of H-bond protons and carbonyl ^{13}C carbons, indicating that the larger shift of the ^{13}C π-spin density is produced by a geometrically distorted though slightly weaker H-bond at C4.

4. Conclusion

This EPR/ENDOR investigation of selectively ^{13}C-labeled ubiquinone anion radicals shows the pronounced influence of hydrogen bonds to the oxygens on the electronic g-tensor and the carbonyl ^{13}C-hf tensors. The g-tensor principal value, g_{xx}, is shifted significantly to lower values and the π-spin densities at the carbonyl carbons are substantially increased upon hydrogen bond formation. Both effects may be explained by mainly electrostatic interactions between the partially positively charged hydrogen ($H^{\delta+}$) from the H-bond donor (isopropanol) and the electrons of the carbonyl oxygens of the ubiquinone anion radical. Since the H-bond is predominantly formed to the non-bonding oxygen orbitals, their energies are lowered with respect to the half-filled π^*-orbital, which explains the observed reduction of g_{xx}. The electrostatic interaction between $H^{\delta+}$ and the C=O group furthermore leads to increased charge density at the oxygen and to increased spin density at the carbonyl carbon, which can be explained in terms of a simple valence bond scheme [8, 24]. For $UQ_0^{-\bullet}$ two different H-bonds at oxygen 1 and 4 were concluded from the hydrogen bond proton hf tensors and from the carbonyl ^{13}C-hf tensors. The experiments have been supplemented by DFT calculations. Overall a very good agreement between experimentally derived and calculated π-spin densities was found. Also, the effect of hydrogen bonding on the spin density distribution was reproduced quite well by the calculations. For $UQ_0^{-\bullet}$ an influence of the geometry of the hydrogen bond to the carbonyl group next to the methyl group is concluded, indicating a slight out-of-plane orientation.

Interestingly, different hydrogen bonding is found for the terminal electron acceptors, $Q_A^{-\bullet}$ and $Q_B^{-\bullet}$, in the RC of *Rb. sphaeroides* (both are UQ_{10}). $Q_A^{-\bullet}$ exhibits one exceptionally strong H-bond; $Q_B^{-\bullet}$ exhibits two hydrogen bonds of comparable magnitude as found for ubiquinones in protic solvents [8]. This indicates that the strength – and maybe also the geometry – of H-bonds is a major cause to the different functions of Q_A and Q_B in the electron transfer process.

Acknowledgements

The authors are grateful to C. Mioskowksi (Saclay) for helpful discussions and support and to R. Bittl, R. Fiege, and C. Geßner (TU Berlin) for developing the

powder simulation and fitting programs. This work was supported by Deutsche Forschungsgemeinschaft (Sfb 312, TP A4). This work was presented at the occasion of the EMARDIS-97 & Applied EPR workshop organized by Prof. N. D. Yordanov, Sofia-Bojana, June 8–17, 1997.

References

[1] Lubitz W., Abresch E.C., Debus, R.J., Isaacson R.A., Okamura M.Y., Feher G.: Biochim. Biophys. Acta **808**, 464–469 (1985)
[2] Feher G., Isaacson R.A., Okamura M.Y., Lubitz W.: Ser. Chem. Phys., vol. 42, pp. 174–189 Berlin: Springer 1985.
[3] Trumpower B.L. (ed.): Function of Quinones in Energy-Conserving Systems. New York: Academic Press 1982.
[4] Lancaster C.R.D., Ermler U., Michel H. in: Anoxygenic Photosynthetic Bacteria (Blankenship R.E., Madigan M.T., Bauer C.E., eds.), pp. 503–526. Dordrecht: Kluwer 1995.
[5] Brudler R., de Groot H.J.M., van Liemt W.B.S., Steggerda W.F., Esmeijer R., Gast P., Hoff A.J., Lugtenburg J., Gerwert K.: EMBO J. **13**, 5523–5530 (1994)
[6] Breton J., Boullais C., Burie J.-R., Nabedryk E., Mioskowski C.: Biochemistry **33**, 14378–14386 (1994)
[7] van den Brink J.S., Spoyalov A.P., Gast P., van Liemt W.B.S., Raap J., Lugtenburg J., Hoff A.J.: FEBS Lett. **353**, 273–276 (1994)
[8] Isaacson R.A., Abresch E.C., Lendzian F., Boullais C., Paddock M., Mioskowski C., Lubitz W., Feher G. in: The Reaction Center of Photosynthetic Bacteria, Structure and Dynamics (Michel-Beyerle M.-E., ed.), pp. 353–367. Berlin: Springer 1996.
[9] Kropacheva T.N., Raap J., Lugtenburg J., Hoff A.J. in: Photosynthesis: from Light to Biosphere (Mathis P., ed.), vol. I, pp. 527–530. Dordrecht: Kluwer 1995.
[10] Samoilova R.I., Gritsan N.P., Hoff A.J., van Liemt W.B.S., Lugtenburg J., Spoyalov A.P., Tsvetkov Y.D.: J. Chem. Soc. Perkin Trans. 2 **1995**, 2063–2068; Samoilova R.I., van Liemt W.B.S., Steggerda W.F., Lugtenburg J., Hoff A.J., Tyryshkin A.M., Gritsan N.P., Spoyalov A.P.: J. Chem. Soc. Perkin Trans. 2 **1994**, 609–614.
[11] Lendzian F.: Ph. D. Thesis, Freie Universität Berlin, Berlin 1982.
[12] Zweygart W., Thanner R., Lubitz W.: J. Magn. Reson. **109A**, 172–176 (1994)
[13] Atherton N.M.: Principles of Electron Spin Resonance. Chichester: Ellis Horwood 1993.
[14] Rieger P.H.: J. Magn. Reson. **50**, 485–489 (1982)
[15] Fiege R.: Ph. D. Thesis, Technische Universität Berlin, Berlin 1997.
[16] Lendzian F., Sahlin M., MacMillan F., Bittl R., Fiege R., Poetsch S., Sjöberg B.-M., Gräslund A., Lubitz W., Laßmann G.: J. Am. Chem. Soc. **118**, 8111–8120 (1996)
[17] Lubitz W., Lendzian F. in: Biophysical Techniques in Photosynthesis (Amesz J., Hoff A.J., eds.), pp. 255–275. Dordrecht: Kluwer Academic Publishers 1996.
[18] Stone A.J.: Proc. Roy. Soc. A London **271**, 424–434 (1963)
[19] Burghaus O., Plato M., Rohrer M., Möbius K., MacMillan F., Lubitz W.: J. Phys. Chem. **97**, 7639–7647 (1993)
[20] DMOL Release 95.0 Molecular Simulations Inc. 1995.
[21] Perdrew J.P., Wang Y.: Phys. Rev. B **45**, 13244 (1992)
[22] Becke A.D.: J. Chem. Phys. **88**, 2547–2553 (1988)
[23] McConnel H.M., Strathdee J.: J. Mol. Phys. **2**, 129–138 (1959)
[24] MacMillan F., Lendzian F., Lubitz W.: Magn. Reson. Chem. **33**, S81–S93 (1995)
[25] McConnell H.J.: J. Phys. Chem. **24**, 764–766 (1956)
[26] Heller C., McConnell H.M.: J. Chem. Phys. **32**, 1535–1539 (1960)
[27] Freed J.H., Fraenckel G.K.: J. Chem. Phys. **39**, 326–348 (1963)
[28] Freed J.H., Fraenckel G.K.: J. Chem. Phys. **40**, 1815–1829 (1964)
[29] Kropacheva T.N., van Liemt W.B.S., Raap J., Lugtenburg J., Hoff A.J.: J. Phys. Chem. **100**, 10433–10442 (1996)
[30] Karplus M., Fraenckel G.K.: J. Chem. Phys. **35**, 1312–1360 (1961)

[31] Wertz J.E., Bolton J.R., Weil J.A.: Electron Spin Resonance. New York: McGraw-Hill 1994.
[32] Burghaus O.: Ph. D. Thesis, Freie Universität Berlin, Berlin 1991.
[33] Kirste B., Niethammer D., Kurreck H.: Appl. Magn. Reson. **3**, 1–18 (1992)
[34] Mallikan R.S.: J. Chem. Phys. **23**, 1833–1848 (1955)

Author's address: Prof. Dr. W. Lubitz, Max-Volmer-Institut für Biophysikalische Chemie und Biochemie, Technische Universität Berlin, 10623 Berlin, Germany